Funded by the Horizon 2020 Framework Programme of the European Union

Grant Agreement nr.: 687008

Project acronym: GOTSolar

Project full title: New technological advances for the third generation of Solar cells

Deliverable D3.3 – Wide band gap HTMs showing high thermal and chemical stability to guarantee their mechanical robustness (Public)

Start date of the project: 01/01/2016	**Project coordinator name**: Adélio Mendes
Duration of the project: 36 months	**Institution of the Project coordinator:** UPORTO
Period covered by this report: from 1/1/2016 to 31/12/2017	**WP Reference**: WP3
Nr. pages: 17	**WP leader name:** Peter Bäuerle
	Institution of the WP leader: UULM

Funded by the Horizon 2020 Framework Programme of the European Union

Contents

Funded by the Horizon 2020 Framework Programme of the European Union

Introduction

The importance to design and synthesize new hole transport materials (HTM) for application in perovskite solar cells (PSC) has been highlighted in two recent reviews on this topic.[1-2] The necessary properties of new HTMs are therein described as following. The HOMO level should be lower than the valance band of the perovskite light absorber and a sufficient hole mobility of around 10^{-3} $cm^2V^{-1}s^{-1}$ is needed. A high glass transition temperature will be favorable to stabilize the amorphous phase beyond the temperature threshold in the device. If possible it is advised to avoid dopants or additives because they contribute to the degradation of the solar cells.[3] Herein, we will take these principles into account in order to design new classes of HTMs.

Fused 2,2'-bithiophenes have been extensively investigated and used as organic materials (Figure 1).[4-9]

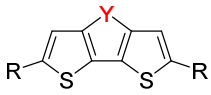

Y=NR, CR_2, SiR_2

Figure 1: Structure of bridged bithiophene.

The spiro-linked cyclopentadithiophene (CPDT) building block has been successfully used in hole transport materials (HTM) in the past (**Figure 2**).[10-11] Spiro-linking also increases the glass transition temperature compared to the normal planar moieties itself.[12]

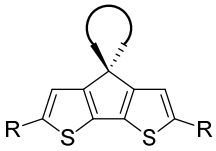

Figure 2: General structure of sprio-cyclopentadithiophenes.

The use of the spiro-bi(cyclopentadithiophene) unit in HTMs, as represented in molecule **UU1** (Figure 3), showed that these materials can give good results and a power conversion efficiency (PCE) of 13.4% without dopants nor additives.[11]

Funded by the Horizon 2020 Framework Programme of the European Union

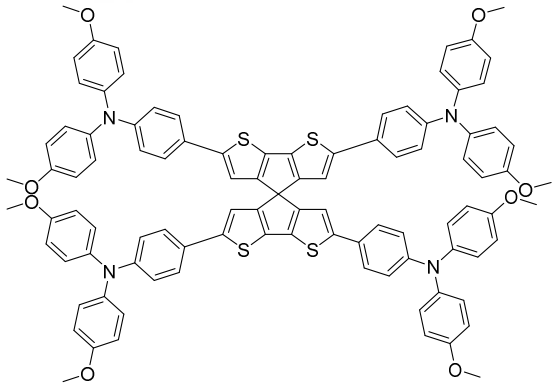

Figure 3: Structure of UU1.

Starting from these promising results, the aim of the project is to design and synthesize novel spiro-CPDTs as central building blocks for HTMs used in perovskite solar cells.

Synthesis

For a first series of large gap HTMs the spiro-CPDT central building block (see **Figure 2**) was proposed. Triarylamines were coupled to the CPDT in order to obtain large-gap HTMs **UU7-UU11**.

Firstly, a synthesis route to the central spiro-CPDT backbone was designed by a retrosynthetic approach. The synthesis was optimized to ensure good reproducible yields.

The first target molecule **UU7**, which comprises the central CPDT unit was attached to *N*,*N*-(*p*-methoxyphenyl)aniline donor-substituents as termini.

For the final cross-coupling step the boronic ester **10** had to be synthesized starting from **8** according to a literature procedure (**Figure 4**).[13-14]

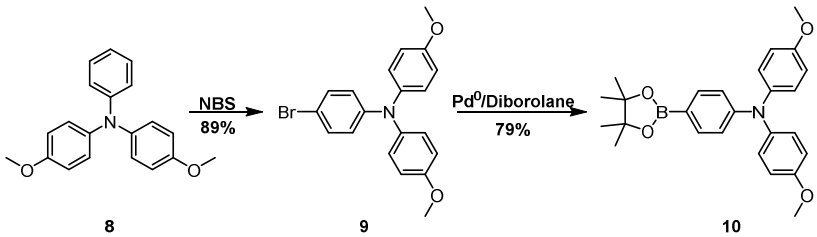

Figure 4: Synthesis of boronic ester 10 via direct borylation.

The boronic ester **10** was coupled to the previously synthesized CPDT central unit utilizing a palladium(0)-catalyzed Suzuki reaction and the HTM **UU7** was obtained.

Another HTM with the spiro-CPDT core was synthesized as a structural comparison to **UU7**. The **UU10** molecule shows the same structural elements as **UU7**, the only difference are the missing methoxy substituents at the triphenylamine substituents. **UU10** was synthesized from the CPDT central unit and boronic ester **11** (**Figure 5**). The missing methoxy groups should lead to a slightly higher HOMO energy level and a larger bandgap for the material **UU10**.

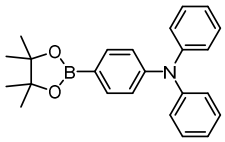

11

Figure 5: Structure of boronic ester 11.

The structure of the next target molecule **UU8**, which comprises a slightly modified central CPDT unit was also terminated by the same *N*,*N*-(*p*-methoxyphenyl)aniline donor substituents, which were used for **UU7**.

The synthetic procedure to HTM **UU8** is quite similar to the **UU7** procedure with a cross-coupling being the last step.

A second CPDT based HTM without methoxy groups at the triphenyl amine substituents was also synthesized. The middle building block was coupled with the boronic ester **11** to generate HTM **UU11.**

The spiro-linkage is often used in structural elements of HTMs. The reason it was introduced first was to generate molecular glasses with high glass transition temperatures.[12, 15] The buildup of spiro-linkage can unfortunately be a complicated synthetic process. Therefore we wanted to create a HTM which shows the desired properties of a spiro-linked material without a spiro-linkage. Therefore a new class of HTMs with a non-spiro core was designed.

The brominated core was obtained in a three step synthesis and was afterwards coupled to the boronic esters **10** and **11** in order to generate the HTMs **UU13** and **UU14** as last series in this

Six wide gap HTMs with three different cores were designed, synthesized and characterized so far. The synthetic steps to the three different middle building blocks have been optimized to ensure good reproducible yields. Further improvements are possible for the final cross-coupling steps especially in the case of **UU13**.

Funded by the Horizon 2020 Framework Programme of the European Union

Optoelectronic characterization

All purified HTMs were investigated using UV-Vis spectroscopy to determine the optical behavior. The absorption maxima $\lambda_{max,abs}$, extinction coefficient ϵ, absorption onset λ_{ons} and the optical band gap $E_{g,opt}$.were determined for each HTM. The optical band gap was calculated with $E_{g,opt} = \frac{hc}{\lambda_{ons}}$ with h being the Planck constant and c being the speed of light in vacuum.

The effect of different arylamine substituents on each of the three previously described middle building blocks was evaluated. The results are summed up at the end of the chapter.

The UV-vis spectra of **UU7** and **UU10** both show two absorption maxima, with the low energy maximum being the most intense one. For **UU7** one absorption maximum at 293 nm and the other at 445 nm were obtained. The maxima for **UU10** are with 287 nm and 436 nm blue-shifted compared to **UU7**. This was expected because of the smaller π-system of **UU10**. The extinction coefficient for **UU10** is around 20% smaller than for **UU7** and it is the smallest one of the series with 55 000 $M^{-1}cm^{-1}$. For **UU7** a band gap of 2.45 eV and for **UU10** 2.51 eV were obtained. The smaller bandgap of **UU7** is again due to the extension of the π-system.

For **UU8** we obtain two and for **UU11** three absorption maxima. The material with the larger π-system, **UU8**, shows again a more red-shifted absorption with the global absorption maximum at 445 nm compared to 437 nm for **UU11**. The extinction coefficients for **UU8** and **UU11** are similar with 68,100 $M^{-1}cm^{-1}$ respectively 67,200 $M^{-1}cm^{-1}$. **UU8** shows the smaller optical bandgap with 2.44 eV compared to 2.51 eV for **UU11**.

The last series of HTMs **UU13** and **UU14** consist of a non-spiro core. **UU13** shows two, **UU14** three absorption maxima with the most redshifted absorption at 443 nm for **UU13** and 435 nm for **UU14**. Both materials show comparable extinction coefficients with 62,600 $M^{-1}cm^{-1}$ for **UU13** and 62,100 $M^{-1}cm^{-1}$ for **UU14**. The optical band gap is 2.47 eV for **UU13** and 2.52 eV – the largest of the whole series – for **UU14**.

The summarized optical data for all synthesized materials and **UU1** as comparison is shown in **Table 1**.

Funded by the Horizon 2020 Framework Programme of the European Union

Table 1: Summary of the optical data for all synthesized HTMs and UU1 for comparison.

	$\lambda_{max,abs}[nm]$	$\varepsilon_{max}\ [M^{-1}cm^{-1}]$	$\lambda_{onset}\ [nm]$	$E_{g,opt}\ [eV]$
UU1	304, 447	100,300	510	2.43 eV
UU7	293, 445	65,000	507	2.45 eV
UU8	289, 445	68,100	510	2.44 eV
UU10	287, 436	55,600	493	2.51 eV
UU11	284, 305, 437	67,200	494	2.51 eV
UU13	300, 443	62,600	502	2.47 eV
UU14	282, 307, 435	62,100	492	2.52 eV

All materials show comparable optical behavior with absorption maxima between 435 nm and 445 nm and extinction coefficients from 55,600 $M^{-1}cm^{-1}$ to 68,100 $M^{-1}cm^{-1}$.The absorption onset lies in the range from 492 nm to 510 nm which corresponds to optical bandgaps between 2.52 eV to 2.44 eV. All molecules are therefore large-gap materials. The materials can be divided into two categories depending whether methoxy substituents were used (**UU7**, **UU8**, and **UU13**) or not (**UU10**, **UU11**, and **UU14**). The first group shows a more red-shifted absorption with maxima between 443 nm and 445 nm and band gaps between 2.47 eV and 2.44 eV. The second group has more blue-shifted maxima between 435 nm and 437 nm as well as larger band gaps between 2.52 eV and 2.51 eV.

Cyclic voltammetry (CV) was performed to determine the oxidation potentials and the energy level of the frontier molecular orbitals. This step is crucial to determine the applicability of the materials in state of the art perovskite solar cells. CV was measured in dichloromethane (DCM) at room temperature using tetrabutylammonium hexafluorophosphate as conducting salt. Three cycles were measured with a scan speed of 100 mV/s. The second scan of each measurement is shown. All potentials are internally referenced to the ferrocene/ferrocenium redox-pair. The HOMO energy level was determined by the onset value of the oxidation (Fc_{HOMO}=-5.1 eV).

UU7 and **UU10** both show two reversible and one quasi reversible oxidations. The oxidation potentials for **UU7** are slightly more negative than for **UU10** and lie at 0.01 V, 0.13 V, and 0.71 V. The first two oxidations are overlapping and the exact positions were therefore evaluated with the help of a time-semi-derivative. The third oxidation of **UU7** seems to be larger than the first two. Integration of the current with respect to the time gave the transferred charge of the oxidation respectively reduction. The transferred current of the first two oxidations is equal to the third oxidation. The third oxidation therefore corresponds to a transfer of two electrons, under the assumption that the first two oxidations correspond to a one electron oxidation. **UU10** shows oxidations at 0.06 V, 0.20 V, and 0.67 V. Each of the oxidations corresponds to a one electron oxidation. For **UU7** we obtain a HOMO of -5.03 eV against vacuum. For **UU10** we obtain a slightly stabilized HOMO of -5.09 eV. The difference between the two molecules can again be attributed to the influence of methoxy groups on the π-system.

The CV of **UU8** shows two reversible and one quasi-reversible oxidations. The oxidation potentials lie at 0.01 V, 0.14 V, and 0.67 V. The onset of a forth, irreversible oxidation is visible for **UU8**. All redox potentials of **UU11** are slightly shifted to more positive values. The oxidations occur at 0.06 V, 0.20 V, and 1.03 V. The third oxidation at 1.03 V is considerably shifted compared to the 0.67 V for the third oxidation of **UU8**. Determination of the HOMO level reveals -5.03 eV for **UU8** and -5.19 eV for **UU11**. The obtained HOMO level for **UU11** could be slightly wrong because of the method of determination via the onset value. The baseline of **UU11** shows a noticeable slope. The first two oxidations of **UU11** are at the same potentials as the **UU10** counterparts. Therefore it is expected, that the **UU11** HOMO lies more in the region of the **UU10** – around -5.09 eV.

For **UU13** three reversible one-electron oxidations can be observed at 0.01 V, 0.14 V, and 0.69 V. The onset of a fourth oxidation is visible. The three oxidation potentials for **UU14** are slightly shifted to positive potentials and lie at 0.10 V, 0.20 V, and 0.98 V. All three oxidations are one-electron oxidations. From the oxidation onset the HOMO energy levels could be calculated to be -5.03 eV for **UU13** and -5.07 eV for **UU14** which is again consistent to the behavior of the two different π-systems.

The electrochemical data is summed up in **Table 2**. The values of **UU1** are also shown for comparison. The HTMs should all be applicable in Perovskite solar cells with these HOMO energy levels. The materials can be divided into two groups, depending on whether methoxy substituents are attached to them or not. The methoxy-substituted group, consisting of **UU7**, **UU8** and **UU13,** generally shows higher HOMO energy levels and the first oxidation takes place at almost 0 V. The second group, consisting of the materials without methoxy substituents, namely **UU10**, **UU11** and **UU14,** shows deeper lying HOMO energy levels than the first group. This could lead to a slightly higher V_{OC} in perovskite solar cells.

Table 2: Summary of the electrochemical data for all synthesized HTMs and UU1 for comparison.

	$E^0_{ox1}\ [V]$	$E^0_{ox2}\ [V]$	$E^0_{ox3}\ [V]$	$HOMO\ [eV]$	$LUMO\ [eV]$
UU1	0.03	0.14	0.67	-5.00	-2.57
UU7	0.01	0.13	0.71	-5.03	-2.58
UU8	0.01	0.14	0.67	-5.04	-2.60
UU10	0.06	0.20	0.67	-5.09	-2.58
UU11	0.06	0.20	1.03	-5.19	-2.68
UU13	0.01	0.14	0.69	-5.03	-2.56
UU14	0.10	0.20	0.98	-5.07	-2.55

Funded by the Horizon 2020 Framework Programme of the European Union

Thermal characterization

All newly developed HTMs were characterized by thermogravimetric analysis (TGA) in order to determine the thermal stability of all materials. Small samples (1-2 mg) of the HTMs were therefore heated to 1000 °C with a heating rate of 10 °C/min and the mass loss was determined. All measurements were carried out under nitrogen atmosphere. The TGA measurements are shown below. Two degradation temperatures were determined, one by the onset of the degredation $T_{deg,ons}$ and one more conservative $T_{dec,5\%}$ which is the temperature at which 5% of the total mass loss (excluding initial weight loss due to solvent evaporation) has occurred.

The TGAs of **UU7** and **UU10** are shown in **Figure 6**. The materials exhibits a total mass loss of 46% for **UU7** and 30% for **UU10** of the initial mass. The decomposition onset was calculated to be 417 °C for **UU7** and 442 °C for **UU10**. The more conservative 5% decomposition temperature lies at 407 °C for **UU7** and 399 °C for **UU10**.

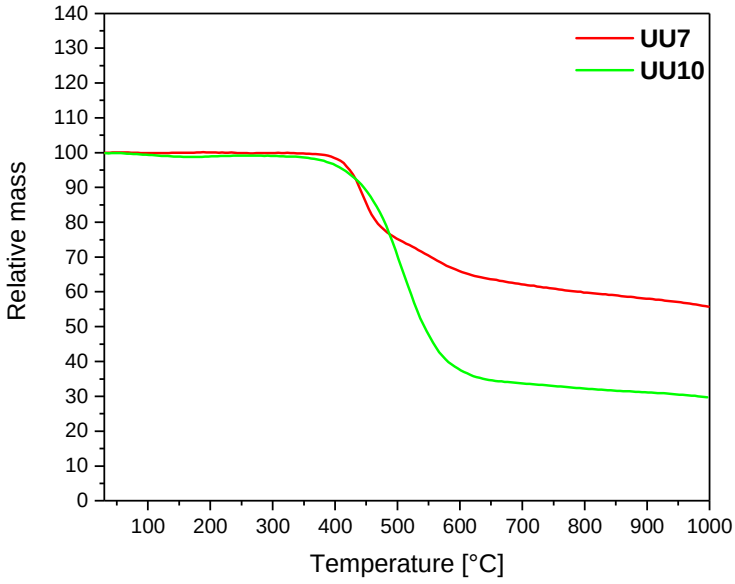

Figure 6: TGA measurements of CPDT HTMs UU7 and UU10.

The TGAs of **UU8** and **UU11** are shown in **Figure 7**. **UU8** exhibits a mass loss of 39% while **UU11** shows a larger mass loss of 63%. The onset decomposition temperature for the two materials are 408 °C for **UU8** and 481 °C for **UU11**. The 5% decomposition is at 408 °C for **UU8** and 439 °C for **UU11**.

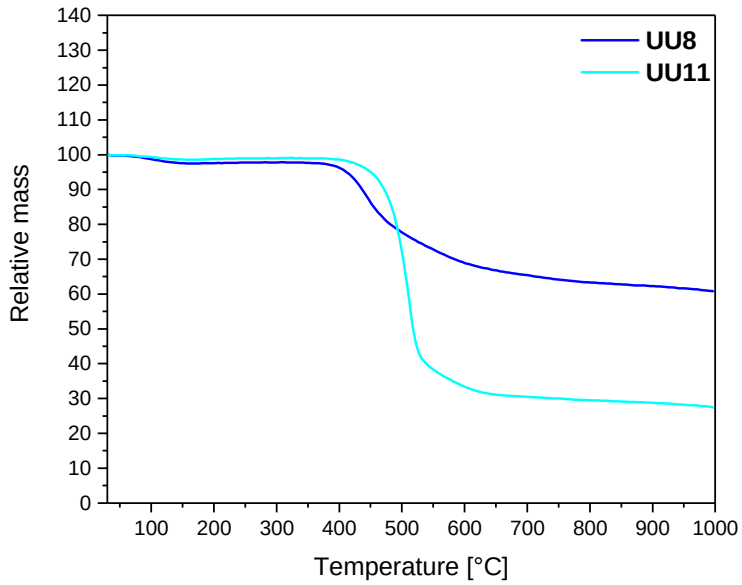

Figure 7: TGA measurements of CPDT HTMs UU8 and UU11.

The TGAs of non-spiro **UU13** and **UU14** are shown in **Figure 8**. **UU13** shows a mass loss of 53% while **UU14** exhibits a loss of 70%. The onset of the decomposition is at 405 °C for **UU13** and 443 °C for **UU14**. The 5% mass-loss happens at 384 °C for **UU13** and 410 °C for **UU14**.

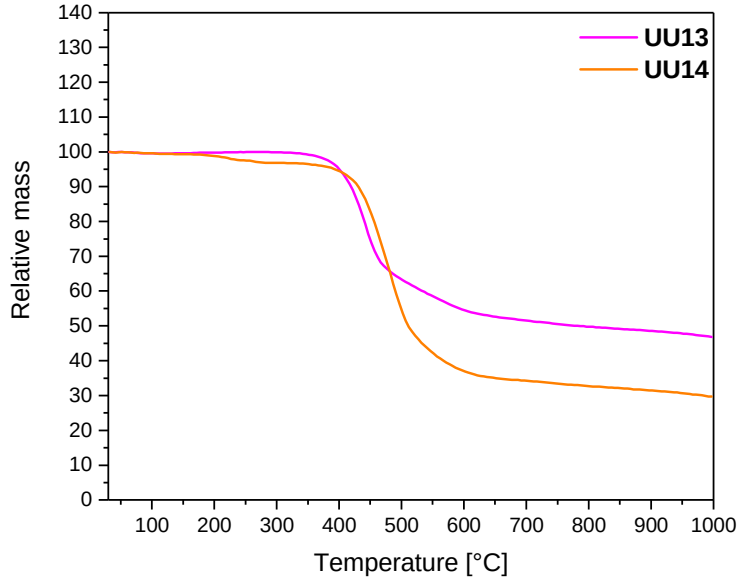

Figure 8: TGA measurements of non-spiro HTMs UU13 and UU14.

All HTMs show a high degree of thermal stability with a start for the degradation (onset) above 400 °C. Therefore no thermal degradation will occur during the procession of the Perovskite solar cells or during illumination. The methoxy-substituted derivatives **UU7**,

UU8, and **UU13** show a smaller degradation temperature and mass loss than the substituted ones. The summarized data is shown in **Table 3**

Table 3: Summarized TGA data of all synthesized HTMs.

	$T_{dec,ons}$ [°C]	$T_{dec,5\%}$ [°C]	Δm[%]	$m_{residue}$[%]
UU7	417	407	44	56
UU8	408	408	39	61
UU10	442	399	70	30
UU11	481	439	63	27
UU13	405	384	53	47
UU14	443	410	70	30

After determination of the degradation temperature differential scanning calorimetry (DSC) was used to determine possible melting temperatures (T_m) and glass transition temperatures (T_g) for all HTMs. The samples of HTM **UU7-UU11** underwent three heating and cooling cycles from 30 °C to 360 °C. The measurements were carried out under argon atmosphere. The scans are ordered downwards.

The DSC of **UU7** is shown in **Figure 9**. All three scans show a variety of signals in the heating cycle. The signals at around 86 °C and 255 °C are artefacts which are also visible if an empty sample is heated. There are no visible signals during the cooling phase. The weak signal at around 168 °C was attributed to a glass transition. The temperature (T_g) was determined by the onset of the phase transition. For the first scan a T_g of 169 °C was obtained. In the second and third scan this temperature was slightly lower with 167 °C, respectively 163 °C. No melting point was observed for **UU7**.

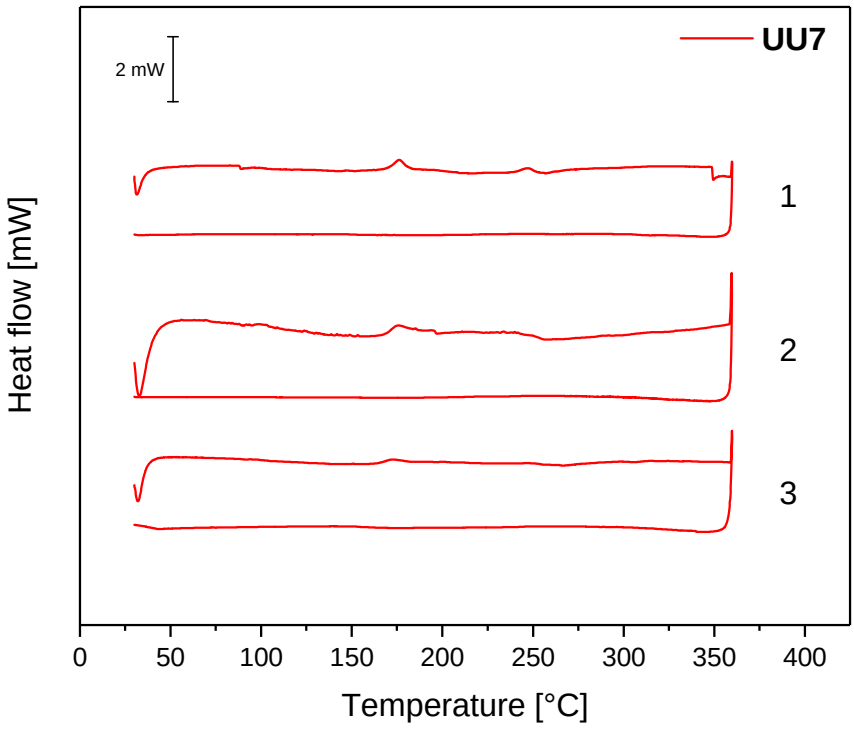

Figure 9: DSC of HTM UU7.

The DSC of **UU8** is shown in **Figure 10**. As in the case of **UU7** a small signal is visible which can be assigned to a glass transition. In the first scan T_g appears at 149 °C, in the second at 152 °C and in the third at 151 °C. No further consistent signal is visible.

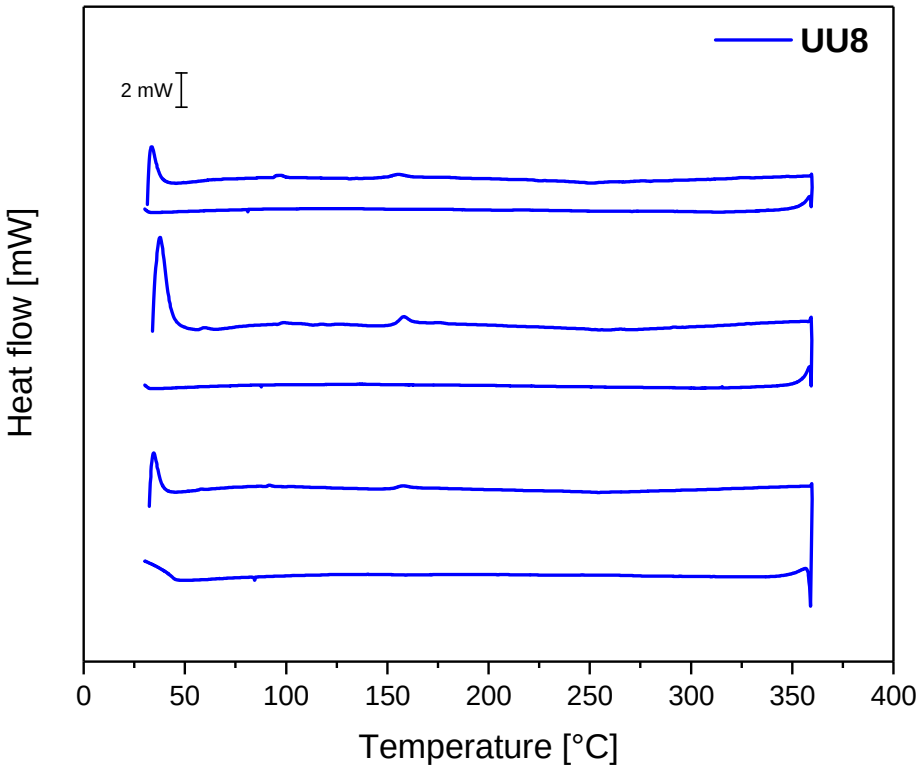

Figure 10: DSC of HTM UU8.

Figure 11 The DSC of **UU10** in **Figure 11** shows again a variety of different signals. The only consistent signal which appears in all three scans is at around 170 °C. The signal is in the same temperature region as for the structural similar **UU7**, therefore it is expected to be T_g. The first scan is unfortunately too inconclusive, therefore the second and third scans were used to determine the temperature. Values of 171 °C, for the first scan, and 168 °C for the second scan, were obtained from the onset.

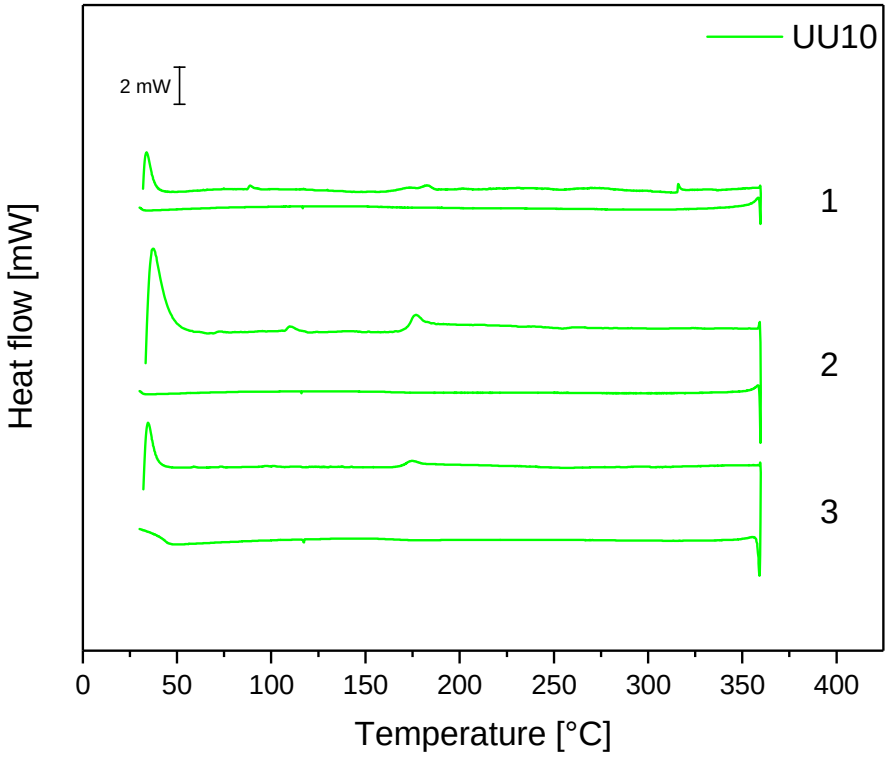

Figure 11: DSC of HTM UU10.

The DSC of HTM **UU11** is shown in **Figure 12**. A large signal is visible in the first scan, which can be assigned to be a melting point. The large melting signal appears in the first scan with an onset value of 302 °C. The first scan shows no T_g for the material. This indicates that the material is in a crystal state after precipitation from solution. After a first melting and cooling cycle the material appears to be in an amorphous state. A glass transition signal is afterwards visible in the second and third heating cycle. T_g was determined to be 167°C for the second and 165 °C for the third cycle.

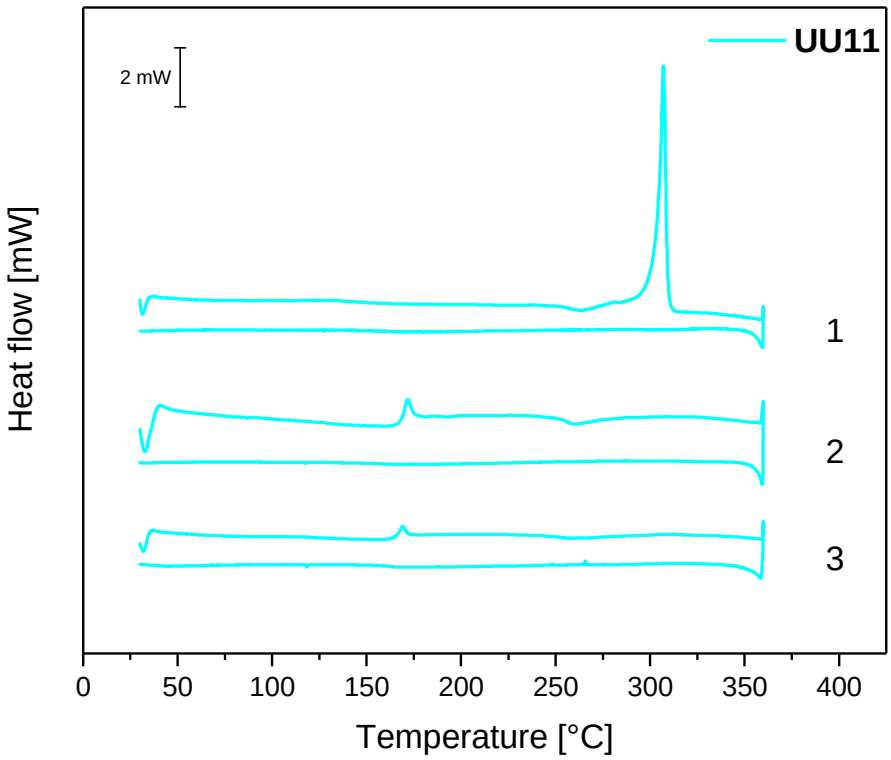

Figure 12: DSC of HTM UU11.

For the last series of HTM **UU13** and **UU14** only two heating and cooling cycles were measured. The DSC of **UU13** is shown in **Figure 13**. In the first heating cycle a melting signal is visible. A melting point of 264 °C was calculated from the onset. A glass transition is visible in the second heating cycle with an onset of 141 °C – the smallest T_g of all measured HTMs. The combination of a melting point in the first heating cycle and a glass transition in the second cycle suggest, that this material also is crystalline after precipitation from solution and the amorphous state is only obtained after one heating and cooling cycle. No melting point was observed for the amorphous state.

Funded by the Horizon 2020 Framework Programme of the European Union

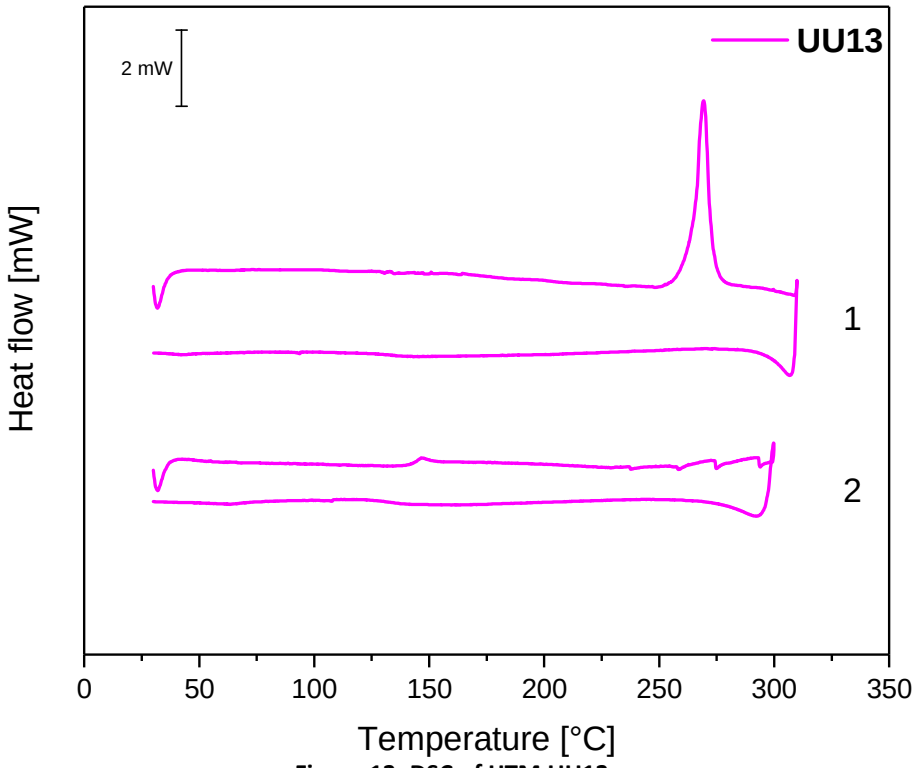

Figure 13: DSC of HTM UU13.

The DSC for the last material, **UU14** is shown below in **Figure 14**. The Material exhibits the same thermal behavior as **UU13**. In the first cycle a melting signal is clearly visible with an onset of 281 °C. In the second cycle a glass transition appears at 148 °C.

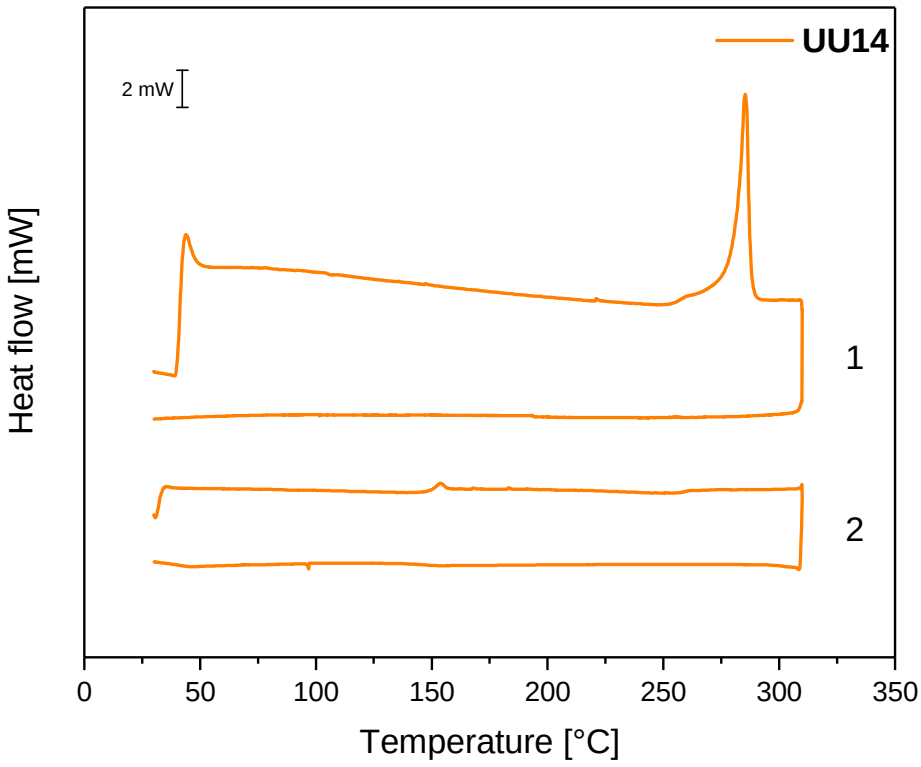

Figure 14: DSC of HTM UU14.

Categorizing the materials reveals two trends for the thermal behavior of the materials. The glass transition temperature increases with increasing size of the backbone. The non-spiro linked CPDT exhibit the lowest T_g for the series. The influence of the methoxy-substituents is also clearly visible. All materials whith methoxy groups exhibit a lower T_g and even a lower melting point (if the melting point is visible) than their unsubstituted counterparts. The melting- and glass transition temperatures are summarized in Table 4.

Table 4: Summarized DSC data for HTMs UU7-UU14.

	T_g [°C]	T_m [°C]
UU7	165	-
UU8	151	-
UU10	170	-
UU11	166	302
UU13	141	264
UU14	148	281

Summary

In the reporting period, we have been working on the development and synthesis of novel hole transport materials for perovskite solar cells. We have successfully synthesized six new large gap HTMs (**UU7**, **UU8**, **UU10**, **UU11**, **UU13** and **UU14.**) and characterized all materials with the help of UV-vis spectroscopy, cyclic voltammetry, thermogravimetric analysis and differential scanning calorimetry. The obtained properties suggest an applicability in state of the art PSC. The HOMO energy levels between -5.03 eV and -5.19 eV are in the right range with respect to the valence band of the perovskite. The high glass transition temperatures and thermal stability until 400 °C look promising in respect to solar cell stability.

Funded by the Horizon 2020 Framework Programme of the European Union

References

[1] C. H. Teh, R. Daik, E. L. Lim, C. C. Yap, M. A. Ibrahim, N. A. Ludin, K. Sopian, M. A. Mat Teridi, *J. Mater. Chem. A* **2016**, *4*, 15788-15822.

[2] L. Calió, S. Kazim, M. Grätzel, S. Ahmad, *Angew. Chem. Int. Ed.* **2016**, *55*, 14522-14545.

[3] S. N. Habisreutinger, T. Leijtens, G. E. Eperon, S. D. Stranks, R. J. Nicholas, H. J. Snaith, *Nano Lett.* **2014**, *14*, 5561-5568.

[4] G. Lu, H. Usta, C. Risko, L. Wang, A. Facchetti, M. A. Ratner, T. J. Marks, *J. Am. Chem. Soc.* **2008**, *130*, 7670-7685.

[5] A. Berlin, G. Zotti, G. Schiavon, S. Zecchin, *J. Am. Chem. Soc.* **1998**, *120*, 13453-13460.

[6] H. Mo, K. R. Radke, K. Ogawa, C. L. Heth, B. T. Erpelding, S. C. Rasmussen, *Phys. Chem. Chem. Phys.* **2010**, *12*, 14585-14595.

[7] A. Yassin, T. Rousseau, P. Leriche, A. Cravino, J. Roncali, *Sol. Energy Mater. Sol. Cells* **2011**, *95*, 462-468.

[8] M. Weidelener, C. D. Wessendorf, J. Hanisch, E. Ahlswede, G. Gotz, M. Linden, G. Schulz, E. Mena-Osteritz, A. Mishra, P. Bäuerle, *Chem. Commun.* **2013**, *49*, 10865-10867.

[9] J. Wu, Y. Ma, N. Wu, Y. Lin, J. Lin, L. Wang, C.-Q. Ma, *Org. Electron.* **2015**, *23*, 28-38.

[10] M. Saliba, S. Orlandi, T. Matsui, S. Aghazada, M. Cavazzini, J.-P. Correa-Baena, P. Gao, R. Scopelliti, E. Mosconi, K.-H. Dahmen, F. De Angelis, A. Abate, A. Hagfeldt, G. Pozzi, M. Graetzel, M. K. Nazeeruddin, *Nat. Energy* **2016**, *1*, 15017.

[11] M. Franckevicius, A. Mishra, F. Kreuzer, J. Luo, S. M. Zakeeruddin, M. Gratzel, *Mater. Horiz.* **2015**, *2*, 613-618.

[12] U. Bach, K. De Cloedt, H. Spreitzer, M. Grätzel, *Adv. Mater.* **2000**, *12*, 1060-1063.

[13] K. Rakstys, A. Abate, M. I. Dar, P. Gao, V. Jankauskas, G. Jacopin, E. Kamarauskas, S. Kazim, S. Ahmad, M. Grätzel, M. K. Nazeeruddin, *J. Am. Chem. Soc.* **2015**, *137*, 16172-16178.

[14] L. Chen, B. Zhang, Y. Cheng, Z. Xie, L. Wang, X. Jing, F. Wang, *Adv. Funct. Mat.* **2010**, *20*, 3143-3153.

[15] J. Salbeck, F. Weissörtel, J. Bauer, *Macromol. Symp.* **1998**, *125*, 121-132.